International Journal of Multiphase Flow 203 (2026) 105854

Contents lists available at ScienceDirect

International Journal of Multiphase Flow

journal homepage: www.elsevier.com/locate/ijmulflow

Research Paper

Improving volume-averaged population balance models for turbulent breakup in liquid–liquid dispersions

Francesco Maluta [a], Gaetano D'Avino [b], Cristian Marchioli [c], Alessandro Paglianti [a], Antonio Buffo [d,*]

[a] Department of Industrial Chemistry "Toso Montanari", Alma Mater Studiorum - Università di Bologna, Via Piero Gobetti 85, 40129, Bologna, Italy
[b] Dipartimento di Ingegneria Chimica, dei Materiali e della Produzione Industriale, Università di Napoli Federico II, P.le Tecchio 80, 80125 Napoli, Italy
[c] Department of Engineering and Architecture, University of Udine, 33100 Udine, Italy, Dipartimento di Fluidodinamica, CISM, Piazza Garibaldi 18, 33100, Udine, Italy
[d] Department of Applied Science and Technology - Institute of Chemical Engineering, Politecnico di Torino, C.so Duca degli Abruzzi 24, Torino, 10129, Italy

ARTICLE INFO

Dataset link: https://doi.org/10.5281/zenodo.18715777

Keywords:
Liquid–liquid dispersions
Population balance modelling
Daughter distribution function
Drop size distribution
Laser diffraction measurements
Stirred tank hydrodynamics
Viscosity effects

ABSTRACT

A volume-averaged population balance model is presented for predicting drop breakup in turbulent liquid–liquid dispersions with varying dispersed-phase viscosity. The approach is based on a zero-dimensional population balance equation and incorporates hydrodynamic information through the cumulative distribution function of the turbulent dissipation rate over the vessel volume, extracted from validated single-phase CFD simulations. Using the cumulative distribution of turbulent dissipation rate, instead of reconstructing its probability density function through histogram binning, yields numerically stable solutions, faster quadrature convergence, and substantially fewer discretization nodes.

The model is evaluated against a dedicated experimental dataset covering nine operating conditions, obtained by combining three dispersed-phase viscosities with three impeller rotation speeds. Drop size distributions were measured, enabling assessment of both moment-based metrics and distribution-level features. Analysis of these data motivated a novel, flexible daughter distribution function based on a weighted sum of two beta distributions. The formulation captures asymmetric and multimodal fragment patterns at high viscosity and improves the representation of the small-diameter region, especially the number-weighted mean size and the left-hand tail, while classical shapes remain adequate at low viscosity.

Across all conditions, the model predicts the Sauter mean diameter with deviations ranging from approximately 5% at low viscosity to about 50% at high viscosity. The increasing discrepancies with viscosity highlight the need for more accurate breakup rate descriptions and for experiments resolving daughter size statistics at high viscosity ratios. Overall, the framework provides a practical route for screening breakup models and for analysing viscosity effects in turbulent dispersions while retaining the full drop size distribution.

1. Introduction

Liquid–liquid dispersions are widely used in extraction and reaction engineering. The interfacial area is controlled by the balance between interfacial forces and turbulent mixing, and it governs mass-transfer and reaction rates (Lohse and Zhang, 2020; Rodriguez et al., 2025). The evolution of the drop size distribution (DSD) reflects a balance between disruptive hydrodynamic contributions and stabilizing interfacial forces, both strongly modulated by fluid properties (Ribeiro et al., 2011; Rodriguez et al., 2025). Among these, viscosity has long been recognized as a key factor: increasing the viscosity of either phase modifies drop deformability, affects breakup time scales, and promotes filament formation and satellite production (Calabrese et al., 1986; Grace, 1982; Stamatoudis and Tavlarides, 1985). These effects intensify under the inhomogeneous turbulence typical of mechanically agitated systems, where distinct flow structures, ranging from inertial eddies to intense shear regions, interact with drops of different sizes (Maaß and Kraume, 2012). Recent studies further show that viscosity can alter the dominant breakup mechanism, shifting from eddy-mediated deformation at low viscosity to elongational stretching at higher viscosity, with enhanced satellite production (Hardy et al., 2025; Carrillo De Hert and Rodgers, 2019, 2018). Steady-state DSDs measured in stirred tanks exhibit a transition from monomodal to bimodal shapes as dispersed-phase viscosity

* Corresponding author.
E-mail addresses: francesco.maluta@unibo.it (F. Maluta), gaetano.davino@unina.it (G. D'Avino), cristian.marchioli@uniud.it (C. Marchioli), alessandro.paglianti@unibo.it (A. Paglianti), antonio.buffo@polito.it (A. Buffo).

https://doi.org/10.1016/j.ijmultiphaseflow.2026.105854
Received 20 February 2026; Received in revised form 2 July 2026; Accepted 22 July 2026
Available online 28 July 2026

increases, with a rapidly growing fraction of satellite drops (Carrillo De Hert and Rodgers, 2018). These findings highlight the need for models that incorporate viscosity-sensitive breakup mechanisms and account for the strong spatial variability of turbulent dissipation within stirred reactors.

Despite extensive research, reliable prediction of DSDs in mechanically agitated systems remains challenging (Solsvik and Jakobsen, 2015). Breakup events occur across a wide range of spatial and temporal scales, and the governing mechanisms depend sensitively on viscosity ratio, turbulence intensity, and local flow topology (Liao and Lucas, 2009; Solsvik et al., 2013). Modest variations in viscosity can lead to qualitatively different fragmentation pathways and markedly different DSDs, especially in the small-d tail where satellite drops accumulate. These complexities make it difficult to transfer breakup models between operating conditions and highlight the need to account for the spatial variability of turbulent dissipation and for the effect of viscosity on breakup.

Accurate DSD measurements are essential for understanding breakup mechanisms and validating population balance models. Over several decades, a broad range of experimental techniques has been developed, differing mainly in image acquisition and drop detection strategies. Early works relied on in-situ probes or endoscopic imaging inside stirred tanks (Kraume et al., 2004; Maaß et al., 2010, 2011; Khalil et al., 2010), often combined with classical image-processing methods such as the Circular Hough Transform (Illingworth and Kittler, 1988; Khalil et al., 2010; Becker et al., 2014). These approaches provide real-time access to the local DSD but are limited by optical distortions, depth-of-field constraints, and reduced sensitivity to the smallest drops. To overcome these issues, ex-situ and sampling-based methods were developed (Desnoyer et al., 2003; EL-Hamouz et al., 2009; Singh et al., 2008, 2009; Carrillo De Hert and Rodgers, 2019), enabling reliable detection of sub-100 μm drops by analysing extracted samples using laser diffraction or high-resolution imaging. Such approaches are particularly valuable in geometries where reflective surfaces, baffles, or small volumes hinder in-situ imaging (Hardy et al., 2025). Advances in pattern-matching algorithms (Maaß and Kraume, 2012) and machine-learning-based detectors (Krizhevsky et al., 2017; Ilonen et al., 2018; Burke et al., 2024) have further improved drop identification, particularly for satellite drops under challenging optical conditions. Recent studies have also leveraged synthetic training data to improve performance (Bana et al., 2024).

Furthermore, the experimental information required to support breakup modelling is inherently distributed across multiple scales. Population-level measurements (Singh et al., 2009; Ribeiro et al., 2011), single-drop visualizations (Maaß et al., 2007; Maaß and Kraume, 2012), and swarm-scale observations (Zhou et al., 2017, 2019, 2021a) each resolve different aspects of the fragmentation process, but direct comparison is hindered by differences in operating conditions, fluid properties, and measurement protocols. In addition, both the operational definition of a breakup event and the procedures used to infer breakup frequencies vary markedly across studies, limiting cross-scale consistency and, in some cases, producing estimates that are incompatible with the PBE framework (Håkansson, 2020). These issues complicate the assessment of breakup kernels and underscore the need for reliable datasets obtained under well-characterized flow conditions that are representative of the target application.

From a modelling standpoint, breakup mechanisms remain challenging to describe. Classical hydrodynamic arguments relate the maximum stable drop size to a balance between turbulent stresses and interfacial tension. In fully turbulent flows, this balance leads to the well-known Hinze scaling, in which the critical diameter scales as $\varepsilon^{-2/5}$, where ε is the turbulent dissipation rate, and depends on a critical Weber number that incorporates material properties (Hinze, 1955). Viscosity further complicates this picture by influencing deformation dynamics and the effective stress balance. Early studies quantified viscous dissipation within the drop and its impact on breakup thresholds (Calabrese et al., 1986). Later work by Davies (1987) and Clark (1988a,b) linked internal viscous damping, deformation time scales, and the transition between inertial and viscous breakup modes, thereby bridging scaling arguments and PBE formulations.

This mechanistic diversity is reflected in the variety of breakup kernels proposed. Turbulent-eddy-interaction models, such as those of Luo and Svendsen (1996) and Martínez-Bazán et al. (1999), emphasize inertial forces or energy transfer, while shear-based or capillary-constraint models, such as those of Lehr et al. (2002) and Zhao and Ge (2007), highlight velocity gradients or interfacial limitations. Hybrid and intermittency-based formulations incorporate turbulence fluctuations or multiscale interactions (Podgórska, 2006; Qi et al., 2020). Reviews by Liao and Lucas (2009) and Solsvik et al. (2013) pointed out the lack of a universal breakup model: kernels calibrated for specific systems may perform poorly when transferred to different geometries, viscosity ratios, or flow regimes.

Viscosity-driven changes in breakup mechanisms introduce further variability. Hardy et al. (2025) showed that increasing the viscosity of the continuous phase can shift breakup from eddy-driven deformation to elongational, wall-driven stretching, producing long filaments and numerous satellites. Similar behaviour occurs for highly viscous dispersed phases (Becker et al., 2014; Solsvik and Jakobsen, 2015; Carrillo De Hert and Rodgers, 2018). Overall, these observations indicate that breakup is strongly conditioned by the local hydrodynamic environment, and that viscosity can modify both breakup thresholds and fragmentation pathways, with the largest discrepancies typically occurring in the small-d tail.

In mechanically agitated dispersions, breakup can be slow compared with turbulent mixing, so drops sample a rapidly renewed local environment that can be described statistically (Bałdyga and Bourne, 1992). The hydrodynamics can then be summarized through hydrodynamic quantities, such as the average turbulent dissipation rate used in the model of Coulaloglou and Tavlarides (1977) or the volume-based turbulent dissipation rate distribution of Buffo et al. (2016), while breakup is modelled independently as a process acting on the evolving size distribution. This decoupled description is most appropriate at low dispersed-phase volume fraction and high mixing intensity, where the hydrodynamics of the dispersed phase has limited influence on the continuous phase (Marchisio and Fox, 2013).

Accordingly, this study proposes a volume-averaged population balance model for predicting drop breakup in turbulent liquid–liquid dispersions. The drop size distribution is assumed to be spatially homogeneous, while the spatial variability of turbulent dissipation rate is retained through the distribution of ε obtained from validated single-phase Computational Fluid Dynamics (CFD) simulations. In this sense, the model is simpler than a spatially resolved CFD–PBM formulation, but it still accounts statistically for the heterogeneous turbulent environment experienced by the drops.

The turbulent dissipation rate distribution is incorporated through its cumulative distribution function (CDF), rather than through a probability density function reconstructed from histogram bins. This extends the volume-averaged approach of Buffo et al. (2016), where the spatial variability of ε was included through a volume-based probability density function. The use of the CDF avoids the sensitivity to histogram discretization associated with PDF reconstruction from CFD cell values, while preserving the advantage of using the full dissipation-rate distribution instead of a single representative value. This choice is also supported by experimental evidence showing that a single representative ε, such as the volume-averaged dissipation rate, and classical Hinze-type arguments are insufficient to reproduce observed DSDs (Carrillo De Hert and Rodgers, 2018, 2019).

Alongside the use of the cumulative distribution of turbulent dissipation rate, a flexible daughter distribution function based on a weighted sum of two beta distributions is introduced. The proposed

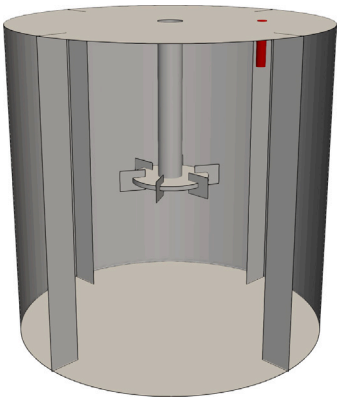

Fig. 1. Geometry of the stirred tank. In red, the position of the sampling tube. (For interpretation of the references to colour in this figure legend, the reader is referred to the web version of this article.)

form preserves mass, accommodates asymmetric or multimodal fragmentation outcomes, and captures satellite formation, which becomes increasingly relevant as viscosity alters breakup mechanisms. The model is assessed using a dedicated dataset comprising nine operating conditions obtained by combining three dispersed-phase viscosities with three impeller speeds. Full DSDs and multiple mean-diameter metrics are available, enabling detailed validation. While previous studies provide phenomenology and empirical correlations (Carrillo De Hert and Rodgers, 2018, 2019), comprehensive datasets explicitly designed for model validation remain comparatively rare. By combining the turbulent dissipation rate distribution with DSD measurements, the present dataset supports evaluation of both distribution-level and moment-based metrics. This enables quantitative assessment of breakup kernels and daughter distribution functions.

The remainder of this manuscript is organized as follows. Section 2 describes the experimental system and measurement procedures. Section 3 presents the population-balance framework, including the use of the cumulative distribution of turbulent dissipation rate and the two-beta daughter distribution function. Section 5 compares predictions and measurements. Section 6 summarizes the main findings and outlines directions for future extensions.

2. The system and the experimental setup

The stirred tank used in this study was previously employed for liquid–liquid investigations (Laurenzi et al., 2009; Maluta et al., 2020). It consists of a cylindrical, flat-bottomed vessel with diameter T and height H, both equal to 232 mm. The tank is equipped with four equally spaced baffles of width $T/10$. Agitation is provided by a single Rushton turbine mounted on a central shaft. The impeller diameter is $D = 76.6\,\text{mm}$ ($D/T = 1/3$) and the off-bottom clearance is $C = T/2$. The liquid height H_L is maintained at H, corresponding to a total volume of 9.8 L. A schematic of the tank is shown in Fig. 1.

The two immiscible liquids are demineralized water, with density $\rho_C = 1000\,\text{kg m}^{-3}$, viscosity $\mu_C = 1 \times 10^{-3}\,\text{Pa s}$, and refractive index $n = 1.33$, and three polydimethylsiloxane (PDMS) silicone oils (Macon Research S.r.l.) with kinematic viscosities and densities, respectively equal to 2 cSt, and $867\,\text{kg m}^{-3}$ (oil_1), 10 cSt, and $941\,\text{kg m}^{-3}$ (oil_2) and 100 cSt, and $974\,\text{kg m}^{-3}$ (oil_3). The interfacial tension for each oil is equal to $\sigma = 0.021\,\text{N m}^{-1}$, and their refractive index is $n = 1.43$. Each experiment was performed by injecting 0.1% vol. of silicone oil into the water-filled tank and agitating at impeller rotational speeds of 500 rpm, 600 rpm, and 700 rpm to ensure complete dispersion. Under these conditions, the flow is fully turbulent, with a rotational Reynolds number between 50 000 and 70 000. By combining three impeller speeds and three viscosities, a total of nine operating conditions were investigated.

The dispersed phase was injected near the impeller using a rigid needle, and each test was allowed to reach steady state for two hours. Local coordinates were defined using a cylindrical reference frame with origin at the tank bottom centre, radial coordinate r directed towards the wall, and axial coordinate z directed upward. Sampling was performed using a rigid PLA tube (inner diameter 7 mm) inserted at $z = 200\,\text{mm}$ and $r/T = 0.28$, while avoiding air entrainment. The influence of tube position, diameter, and withdrawal rate on sample integrity was assessed at the beginning of the campaign.

Drop size distributions were measured using a Spraytec laser-diffraction system (Malvern Panalytical) equipped with a wet dispersion unit. A 100 mL aliquot was collected and immediately transferred to the Spraytec unit. A stirrer recirculated the sample through the measurement cell between transmitter and receiver. Recirculation flow rate, sample volume, and measurement duration were adjusted at each operating condition. Scattered-light patterns were recorded for 30 s and averaged over sliding 10 s windows to obtain a discretized, volume-weighted DSD. The measured drop-size distributions refer to equivalent-sphere diameters. While no direct information on drop shape, deformation, or topology is retained, this approach provides full spectral information across the entire size range, in contrast to the moment-based metrics most commonly reported in the literature. Following Triballier et al. (2003), the use of Lorenz–Mie inversion ensures accurate sizing of fine drops. Obscuration levels were kept below 10%, well below the 60% multiple-scattering threshold, ensuring negligible error from the correction algorithm of the instrument.

For each condition, the mean and coefficient of variation (CoV) of the volume fraction in each size class were determined from several independent acquisitions. To propagate this variability to integral quantities, a Monte Carlo resampling approach was used Ghanem and Doostan (2006) and Rochman et al. (2014). Class-wise volume fractions were perturbed according to their measured CoV, renormalized to preserve total disperse phase volume, and the diameters recomputed for each realization. The 16th–84th percentile of the resulting ensemble was taken as an approximate confidence interval. This procedure assumes largely uncorrelated bin-to-bin variations and captures the dominant experimental uncertainties (sampling, dilution, and optical response) without introducing unrealistic coherent ±CoV perturbations.

3. Mathematical model

As previously mentioned, the evolution of the drop size distribution (DSD) is modelled using a zero-dimensional, volume-averaged population balance framework. A detailed derivation of the governing equations is provided in Buffo et al. (2016). Starting from the definition of the local expected number of drops per unit volume

$$\hat{n}(d, \mathbf{x}, t)\,\mathrm{d}d\,\mathrm{d}\mathbf{x},$$

representing the number of drops with diameter between d and $d + \mathrm{d}d$ located between $\mathbf{x}$ and $\mathbf{x}+\mathrm{d}\mathbf{x}$ at time t, the Population Balance Equation (PBE) describing the evolution of the DSD can be written as (Marchisio and Fox, 2013; Ramkrishna, 2000):

$$\frac{\partial \hat{n}(d, \mathbf{x}, t)}{\partial t} + \nabla \cdot (\mathbf{U}\,\hat{n}(d, \mathbf{x}, t)) = \hat{S}(d, \mathbf{x}, t). \tag{1}$$

The first term on the left-hand side is the accumulation term, the second accounts for convection in physical space, while the source term $\hat{S}$ accounts for changes in the DSD due to breakup. When mixing time scales are shorter than breakup time scales (Buffo et al., 2016), the DSD may be assumed spatially homogeneous. A volume-averaged DSD can then be defined as:

$$n(d, t) = \frac{1}{V}\int_V \hat{n}(d, \mathbf{x}, t)\,\mathrm{d}\mathbf{x}, \tag{2}$$

and by integrating each term of Eq. (1), one obtains:

$$\frac{\mathrm{d}n(d, t)}{\mathrm{d}t} = \frac{1}{V}\int_V \hat{S}(d, \mathbf{x}, t)\,\mathrm{d}\mathbf{x}, \tag{3}$$

where the convective contribution vanishes due to spatial homogeneity. The remaining source term may depend on local flow conditions, particularly the turbulent dissipation rate $\varepsilon(\mathbf{x})$, which varies strongly in stirred tanks. Expressing the source term in terms of the spatial distribution of ε gives:

$$\frac{1}{V}\int_V \hat{S}(d,\mathbf{x},t)\,\mathrm{d}\mathbf{x} = \int_0^\infty S(\varepsilon,d,t)\,f(\varepsilon)\,\mathrm{d}\varepsilon, \tag{4}$$

where $f(\varepsilon)\,\mathrm{d}\varepsilon$ denotes the fraction of tank volume experiencing dissipation rates between ε and $\varepsilon+\mathrm{d}\varepsilon$. The distribution satisfies:

$$\int_0^{+\infty} f(\varepsilon)\,\mathrm{d}\varepsilon = 1, \qquad \int_0^{+\infty} f(\varepsilon)\,\varepsilon\,\mathrm{d}\varepsilon = \bar{\varepsilon}, \tag{5}$$

with $\bar{\varepsilon}$ the volume-averaged dissipation rate.

Eq. (4) shows how breakup kernels can be averaged over the vessel volume by using the distribution of turbulent dissipation rate. If this distribution is introduced through a probability density function, $f(\varepsilon)$ must be reconstructed from the discrete set of CFD cell values, typically by assigning the cell volumes to a finite number of bins. The resulting histogram depends on the selected bin width and bin boundaries. This dependence is most evident in the tails of the dissipation-rate distribution, where only a small number of cells may contribute to each bin, while the breakup kernel can still be sensitive to large values of ε. To avoid this histogram reconstruction, we use the corresponding cumulative distribution function $c(\varepsilon)$ of the turbulent dissipation rate:

$$f(\varepsilon)\,\mathrm{d}\varepsilon = \mathrm{d}c(\varepsilon).$$

Substituting this into Eqs. (3) and (4) yields:

$$\frac{\mathrm{d}n(d,t)}{\mathrm{d}t} = \int_0^1 S(\varepsilon(c),d,t)\,\mathrm{d}c. \tag{6}$$

Eq. (6) shows that the population balance equation is still written for the number density function $n(d,t)$. The cumulative distribution function $c(\varepsilon)$ enters only in the evaluation of the volume-averaged breakup source term, where the integration is performed with respect to the cumulative volume fraction, with fixed limits from 0 to 1, instead of using an approximation of $f(\varepsilon)$ reconstructed from histogram bins. In this way, the numerical evaluation does not require selecting a bin width or bin boundaries for the turbulent dissipation rate distribution. The monotonic behaviour of $c(\varepsilon)$ further improves numerical robustness.

This use of the cumulative distribution function should be distinguished from cumulative or inverse-cumulative formulations of the population balance equation, where the cumulative distribution of the particle size distribution is used as part of the numerical solution strategy (Peterson et al., 2022). Here, the PBE is still solved for the number density function, while the CDF is used only to represent the spatial distribution of turbulent dissipation rate.

With the breakup source term written explicitly, Eq. (6) becomes:

$$\frac{\mathrm{d}n(d,t)}{\mathrm{d}t} = \int_d^{+\infty} \beta(d,l)\,\bar{h}(l)\,n(l,t)\,\mathrm{d}l \;-\; \bar{h}(d)\,n(d,t), \tag{7}$$

where $\beta(d,l)$ is the daughter distribution function (DDF) and the volume-averaged breakup kernel $\bar{h}(d)$ is:

$$\bar{h}(d) = \int_0^1 h(\varepsilon(c);d)\,\mathrm{d}c. \tag{8}$$

This formulation is particularly relevant given that, in stirred tanks, drop sizes and local turbulence conditions do not always fall within the range where inertial-subrange scaling arguments are expected to hold, and viscosity effects further modify the local stress environment (Carrillo De Hert and Rodgers, 2018, 2019). Integrating $h(\varepsilon;d)$ over the full dissipation-rate distribution provides a more consistent representation of the underlying physics than using a single representative ε.

To model the breakup frequency of viscous drops, the kernel proposed by Zhou et al. (2021b, 2022) is adopted:

$$h(\varepsilon,d) = \frac{8\sigma(1+We_{\mathcal{L}})}{C_1\mu_d d + d\sqrt{C_1^2\mu_d^2 + C_2\,8\rho_d\sigma d(1+We_{\mathcal{L}})}} \cdot \frac{2}{\sqrt{\pi}}\Gamma_{upper}\left(\frac{3}{2}, \frac{9C_3}{4We_{\mathcal{L}}} + (2^{5/18}-1)C_4\frac{3Oh}{4\sqrt{We_{\mathcal{L}}}}\right), \tag{9}$$

where $C_1 = 14$, $C_2 = 8$, $C_3 = 0.365$, and $C_4 = 3$ are the parameter values reported by Yu et al. (2025). Here, μ_d and ρ_d are the dispersed-phase viscosity and density, Γ_{upper} denotes the regularized upper incomplete gamma function, and the Ohnesorge number is:

$$Oh = \frac{\mu_d}{\sqrt{\rho_d d\sigma}}. \tag{10}$$

The dependence on ε enters through the integral-length scale Weber number:

$$We_{\mathcal{L}} = \frac{3}{8}(2\pi)^{-2/3}\frac{1.5\rho_c\varepsilon^{2/3}d^{4/3}\mathcal{L}^{1/3}}{\sigma}, \tag{11}$$

where $\mathcal{L}$ is the turbulent integral length scale and is taken here as the impeller height following Zhou et al. (2022). Including $\mathcal{L}$, μ_d, and Oh relaxes the common assumption that breakup is governed solely by inertial-range eddies at the drop scale, as in classical kernels such as those of Coulaloglou and Tavlarides (1977) and Alopaeus et al. (2002), and explicitly accounts for viscous damping effects in the breakup frequency. Additionally, drop deformation is not explicitly resolved in the present framework, which is formulated in terms of equivalent diameters. Capturing three-dimensional drop morphology would require resolved experimental or numerical data and is outside the scope of the present work.

A comparison between this kernel and those of Coulaloglou and Tavlarides (1977) and Alopaeus et al. (2002) is shown in Fig. 2, for oil_1 and oil_3, at a representative dissipation rate $\varepsilon = 10\ \mathrm{m^2\,s^{-3}}$. Fig. 2 shows that the Coulaloglou and Tavlarides model is effectively insensitive to dispersed-phase viscosity: the predicted curves nearly coincide for the two oils. In contrast, the Alopaeus kernel captures the expected viscosity dependence, with breakup frequency decreasing as dispersed-phase viscosity increases; at low viscosity it converges towards the Coulaloglou and Tavlarides prediction, whereas at higher viscosity it yields smaller frequencies at fixed drop diameter. The kernel by Zhou et al. (2022), referred to as the Zhou kernel hereinafter, exhibits a similar qualitative viscosity dependence but predicts substantially lower breakup frequencies in the drop size range relevant to the present study. In particular, the breakup frequency approaches zero at a diameter of about 0.3 mm. For reference, the Kolmogorov length scale under these conditions is approximately 20 μm, suggesting that breakup occurs primarily in the inertial subrange. The markedly smaller breakup rates predicted by the formulation of Zhou et al. (2022) imply slower approach to steady state, an aspect not investigated experimentally here but suitable for future time-resolved studies coupling modelling and measurement. Finally, the Zhou et al. (2022) kernel does not include an explicit dependence on continuous-phase viscosity. This limitation is not critical for the present dataset, where water was used as the continuous phase in all experiments, but it becomes relevant when extending the framework to systems in which the continuous-phase viscosity is varied. Continuous-phase viscosity can change the breakup pathway from drop–eddy interactions to filament stretching and satellite formation (Hardy et al., 2025). Therefore, future extensions should consider the role of both phase viscosities, supported by dedicated experiments in which the continuous-phase viscosity is varied systematically.

Another important aspect in modelling drop breakup is the DDF $\beta(d,l)$. In our previous work (Maluta et al., 2021b), we critically assessed different DDF shapes and showed that the expression providing the best agreement with experiments is the one describing the formation of multiple daughters from a single mother drop. This behaviour has been recently confirmed by both numerical and experimental studies (Farsoiya et al., 2023; Carrillo De Hert and Rodgers, 2018). Although debate persists regarding whether DDFs should be U-shaped, bell-shaped, M-shaped, or multimodal (Liao and Lucas, 2009), it is now evident that the breakup outcome is strongly influenced by the local hydrodynamics (Farsoiya et al., 2023). As a result, different

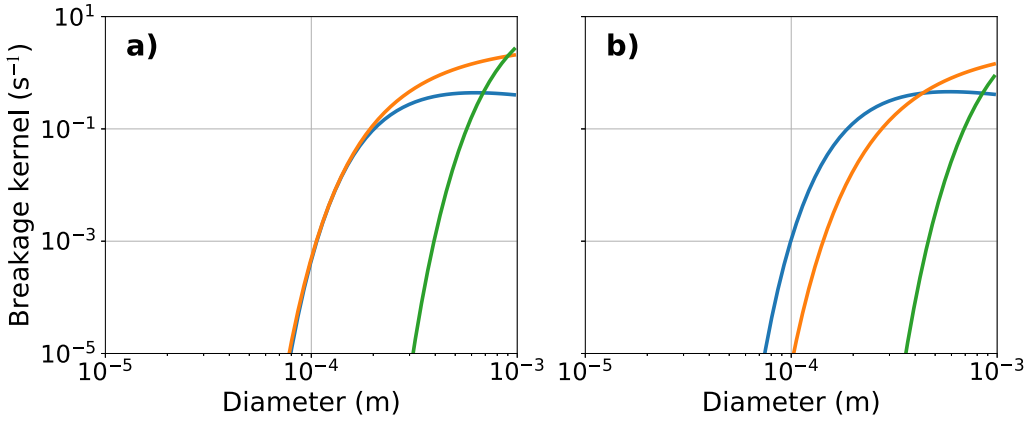

Fig. 2. Breakup frequency from three literature kernels as a function of mother drop diameter. Blue line: Coulaloglou and Tavlarides (1977); orange line: Alopaeus et al. (2002); green line: Zhou et al. (2021b, 2022). Water–oil system at $\varepsilon = 10$ m^2 s^{-3}. Panels: (a) oil_1; (b) oil_3. (For interpretation of the references to colour in this figure legend, the reader is referred to the web version of this article.)

daughter size patterns and thus different DDF shapes can arise under different local flow conditions. In stirred tanks, where the hydrodynamic environment varies widely in space and time, adopting a single prescribed DDF shape is therefore unlikely to be universally adequate. Several phenomenological DDFs have been proposed in the literature (Liao and Lucas, 2009), in which the distribution shape is expressed as a function of local hydrodynamic variables. However, these formulations are typically developed and calibrated under specific conditions, and they do not account for the wide range of hydrodynamic variability encountered in practical agitated reactors. For this reason, the present work adopts a statistical approach in which the DDF does not depend explicitly on hydrodynamic variables. A new, flexible DDF is introduced that satisfies the usual requirements, i.e., its zeroth- and third-order moments match the total number of fragments and the mother volume, while retaining sufficient flexibility to represent different fragmentation mechanisms. Specifically, a weighted sum of two beta probability density functions is considered:

$$\beta(x) = N_s p_s(x) + N_l p_l(x), \qquad x \in (0,1) \tag{12}$$

where x is the daughter-to-mother volume ratio ($x = V_d/V_m$), N_s and N_l denote the number of small and large daughters, and p_s and p_l are normalized beta distributions:

$$p_i(x) = \frac{x^{\alpha_i - 1}(1-x)^{\beta_i - 1}}{B(\alpha_i, \beta_i)}, \qquad i \in \{s, l\}. \tag{13}$$

The normalization factor is:

$$B(\alpha, \beta) = \frac{\Gamma(\alpha)\Gamma(\beta)}{\Gamma(\alpha + \beta)}. \tag{14}$$

The parameters α_i and β_i are expressed in terms of two physically interpretable quantities:

$$\alpha_i = \kappa_i \mu_i, \qquad \beta_i = \kappa_i (1 - \mu_i), \tag{15}$$

where μ_i represents the mean daughter-to-mother volume ratio for group i and κ_i controls the width of the distribution (larger κ_i yields narrower distributions). Conservation of total fragment number and mother volume imposes a constraint between μ_s and μ_l, so that only one of them can be independently selected:

$$\mu_l = \frac{1 - N_s \mu_s}{N_l}. \tag{16}$$

With the five parameters $\{N_s, N_l, \mu_s, \kappa_s, \kappa_l\}$, this DDF can represent a wide range of observed breakup outcomes, from symmetric binary splits to highly skewed fragmentation with numerous small daughters. Examples of the distributions generated by this parametrization are shown in Fig. 3. The figure illustrates how the proposed DDF $\beta(x)$ covers different breakup behaviours. In the left panel, three representative regimes are shown: a U-shaped density that concentrates probability near extreme splits $x \to 0, 1$ (blue line), a symmetric bell-shaped density peaked at $x \approx 0.5$ (orange line), and an M-shaped, bimodal density with two interior modes and a trough near $x \approx 0.5$ (green line). In the right panel, enforcing two large fragments ($N_l = 2$) together with many small ones produces highly skewed multimodal distributions with sharp peaks at small x; increasing N_s and decreasing μ_s shifts probability towards smaller daughter fractions and accentuates these peaks. The green (binary, M-shaped) and black (ten-fragment) curves are included only as illustrative examples of the parametrization; the remaining curves are those used to model breakup in the present systems. Overall, the parametrization provides a consistent way to represent daughter size distributions across breakup regimes that vary with viscosity and local dissipation, while remaining compatible with the population balance formulation used here.

4. Numerical details

4.1. Description of the CFD setup

To obtain the volume-weighted cumulative distribution function of ε, $c(\varepsilon)$, single-phase RANS simulations were performed in OpenFOAM 11. The flow field was computed by solving the steady, incompressible Reynolds-averaged Navier–Stokes equations:

$$\nabla \cdot \mathbf{u} = 0, \tag{17}$$

$$\rho_C (\mathbf{u} \cdot \nabla)\mathbf{u} = -\nabla p + \nabla \cdot \left[(\mu_C + \mu_t)(\nabla \mathbf{u} + \nabla \mathbf{u}^T) \right], \tag{18}$$

where $\mathbf{u}$ is the mean velocity, p the pressure, and μ_t the eddy viscosity. Turbulence was modelled using the standard k–ε formulation:

$$\nabla \cdot (\rho_C k \mathbf{u}) = \nabla \cdot \left[\left(\mu_C + \frac{\mu_t}{\sigma_k} \right) \nabla k \right] + P_k - \rho_C \varepsilon, \tag{19}$$

$$\nabla \cdot (\rho_C \varepsilon \mathbf{u}) = \nabla \cdot \left[\left(\mu_C + \frac{\mu_t}{\sigma_\varepsilon} \right) \nabla \varepsilon \right] + C_{1\varepsilon} \frac{\varepsilon}{k} P_k - C_{2\varepsilon} \rho_C \frac{\varepsilon^2}{k}, \tag{20}$$

where k and ε are the turbulent kinetic energy and its dissipation rate, and the turbulence production term is $P_k = 2\mu_t E_{ij} E_{ij}$ with $E_{ij} = \frac{1}{2}(\partial_i u_j + \partial_j u_i)$. The turbulent viscosity is $\mu_t = \rho_C C_\mu k^2/\varepsilon$, with model constants $C_\mu = 0.09$, $C_{1\varepsilon} = 1.44$, $C_{2\varepsilon} = 1.92$, $\sigma_k = 1.0$, and $\sigma_\varepsilon = 1.3$. Impeller rotation was treated using the steady Multiple Reference Frame (MRF) approach. No-slip boundary conditions were applied to all solid surfaces, including the top, since the experimental tank is equipped with a lid; zero-normal-gradient conditions were used for k, ε, and p.

The mesh consisted of approximately 5.5×10^6 hexahedral cells, with a characteristic spacing $h = 0.8$ mm near the blades. Second-order schemes were employed for spatial discretization. Grid convergence was assessed using three systematically refined meshes and the

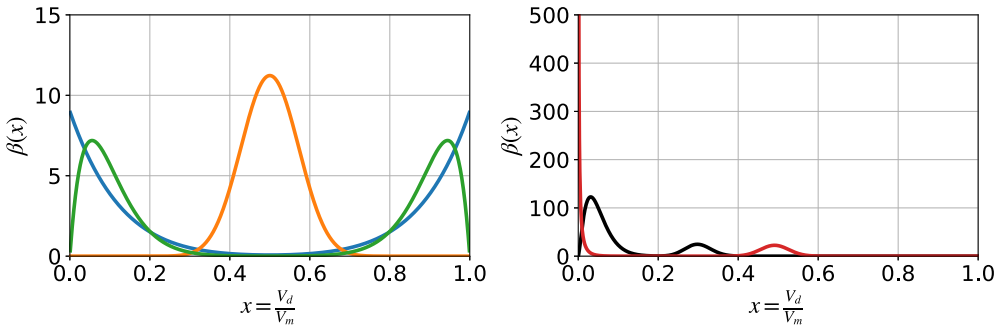

Fig. 3. Left panel: three daughter distribution functions for binary breakup. Blue line (U-shape) with $N_s = 1$, $N_l = 1$, $\mu_s = 0.1$, $\kappa_s = 10$ and $\kappa_l = 10$; orange line (bell-shape) with $N_s = 1$, $N_l = 1$, $\mu_s = 0.5$, $\kappa_s = 50$ and $\kappa_l = 50$; green line (M-shape) with $N_s = 1$, $N_l = 1$, $\mu_s = 0.1$, $\kappa_s = 20$ and $\kappa_l = 20$. Right panel: DDF for two large daughters and varying numbers of small ones. Red line with $N_s = 8$, $N_l = 2$, $\mu_s = 0.05$, $\kappa_s = 50$ and $\kappa_l = 200$; black line with $N_s = 18$, $N_l = 2$, $\mu_s = 10^{-4}$, $\kappa_s = 50$ and $\kappa_l = 200$. (For interpretation of the references to colour in this figure legend, the reader is referred to the web version of this article.)

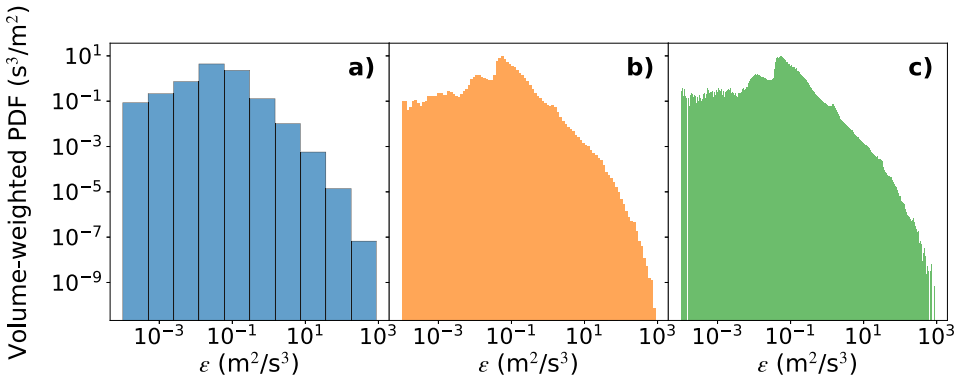

Fig. 4. Discretized volume-weighted probability density function of turbulent dissipation rate inside the stirred tank for different numbers of bins N at 500 rpm. Left: $N = 10$; centre: $N = 100$; right: $N = 1000$.

Table 1
Grid-convergence verification of the single-phase hydrodynamic simulation at 500 rpm. The verification quantity is the dissipation-based power number $N_P^\epsilon = P_\epsilon/(\rho N^3 D^5)$. The Richardson-extrapolated value is $N_{P,\text{ext}}^\epsilon = 4.97$.

Grid	Cells	h [mm]	N_P^ϵ [–]	GCI [%]
G1	5.5×10^6	0.80	4.86	2.79
G2	2.2×10^6	1.10	4.60	9.48
G3	0.60×10^6	1.60	3.71	34.06

dissipation-based power number, $N_P^\epsilon = P_\epsilon/(\rho N^3 D^5)$, as the verification quantity, where P_ϵ is obtained from the volume integral of the turbulent dissipation rate. The results of this study are reported in Table 1. The three-grid sequence showed monotonic convergence from $N_P^\epsilon = 3.71$ on the coarsest grid to $N_P^\epsilon = 4.86$ on the finest grid, with a Richardson-extrapolated value $N_{P,\text{ext}}^\epsilon = 4.97$. The corresponding grid convergence index (GCI) decreased from 34.06% on the coarsest grid to 2.79% on the finest grid. The finest grid, G1, was therefore selected for generating the turbulent-dissipation cumulative distribution functions used in the population-balance calculations. Previous analyses showed that N_P^ϵ obtained with the finest mesh differed by less than 3% from the experimental value. Local velocity fluctuations and dissipation profiles were in reasonable agreement with the measurements of Baldi et al. (2004) and Escudié and Liné (2003), consistent with the limitations of steady MRF–RANS modelling (Maluta et al., 2021a).

The validity of neglecting the dispersed phase in the CFD simulations was confirmed experimentally in Maluta et al. (2021a), where PIV measurements in single-phase water and in dilute (0.1 vol%) diesel–water dispersions showed overlapping mean and fluctuating velocity profiles. The single-phase ϵ field is therefore considered representative of the continuous-phase hydrodynamics in the dilute systems examined.

From the CFD results, the volume-averaged dissipation rates were $\bar{\epsilon} = 0.75\,\text{m}^2\,\text{s}^{-3}$, $1.31\,\text{m}^2\,\text{s}^{-3}$, and $2.08\,\text{m}^2\,\text{s}^{-3}$ at 500 rpm, 600 rpm, and 700 rpm, respectively. Fig. 4 shows volume-weighted PDFs of ϵ constructed using different numbers of bins N. Increasing N increases the resolution of the histogram but also amplifies statistical noise, especially in the tails. By contrast, Fig. 5 shows the cumulative distribution function $c(\epsilon)$ obtained directly from the CFD cell values, yielding a smooth and strictly monotonic function suitable for evaluating the integral in Eq. (6) with a robust numerical quadrature. As shown in Fig. 5, the distributions are similar across the three impeller speeds, while increasing rotation shifts the curve towards higher dissipation levels.

4.2. Details on the solution of the PBE

Eq. (7) was solved for the number density function $n(d,t)$ using the fixed-pivot method of Kumar and Ramkrishna (Ramkrishna, 2000). The size coordinate was discretized into 45 classes between 1 μm and 1 mm, matching the 45 size classes provided by the static light-scattering instrument and enabling direct comparison between numerical and experimental DSDs. This discretization concerns the drop size distribution and is distinct from the numerical treatment of the turbulent dissipation rate distribution. The initial DSD was taken as a Dirac delta centred in the largest size class. Time integration was performed using a high-order backward differentiation formula as implemented in `scipy`. The breakup rate integral in Eq. (8) was evaluated using Gauss–Legendre quadrature with 50 nodes, after piecewise-linear interpolation of the cumulative distribution function of turbulent dissipation rate constructed directly from all CFD cell values. In this way, the volume-averaged breakup frequency is evaluated without histogram binning of the dissipation-rate distribution. The number of quadrature nodes was selected based on the error analysis reported in the following section.

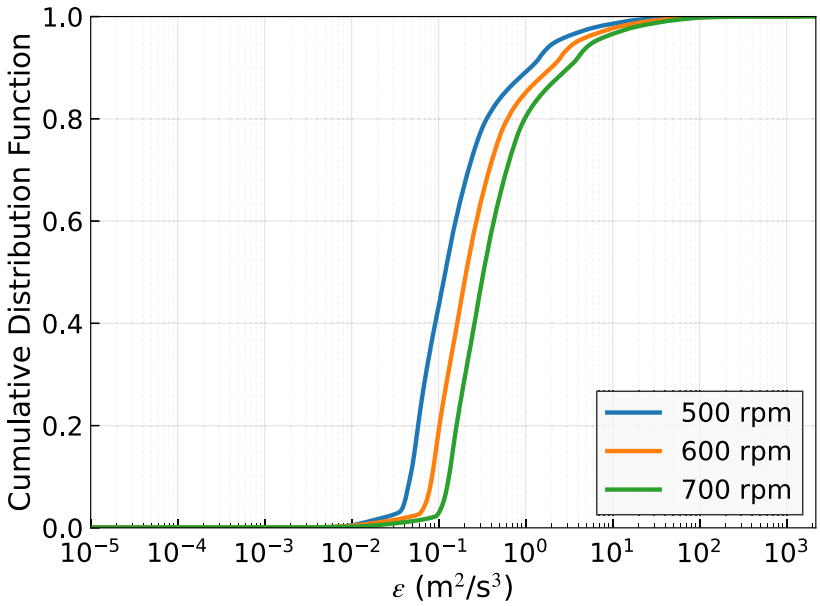

Fig. 5. Volume-weighted cumulative distribution function of turbulent dissipation rate for three impeller speeds.

Final simulation times were selected based on time-sensitivity tests, and steady state was assumed once the relative change in the Sauter mean diameter between two consecutive time steps fell below 1%. The code was written in Python and is available on Zenodo, together with the data reported in this work (Maluta et al., 2026).

5. Results

5.1. Comparison between PDF and CDF approaches

Before solving Eq. (7), the numerical evaluation of Eq. (8) was assessed by comparing two ways of treating the turbulent dissipation rate distribution: reconstruction of its probability density function through histogram binning, as in Buffo et al. (2016), and direct use of its cumulative distribution function. In the PDF-based evaluation, changing the number of bins modifies both the resolution of the dissipation-rate distribution and the statistical noise in each bin, particularly in the high-ϵ tail. The CDF-based evaluation avoids this choice because the cumulative distribution is constructed directly from the ordered CFD cell values. Fig. 6 reports the relative error in the averaged breakup frequency $\bar{h}(d)$ at a fixed droplet diameter, as a function of the PDF bin count N and the number of quadrature nodes used in the CDF formulation. The reference value of $\bar{h}(d)$ was obtained by integrating over a CDF constructed directly from all CFD cell values, i.e., without binning. For comparable discretization sizes, using the cumulative distribution of ε gives errors that are approximately two orders of magnitude smaller than those obtained when the probability density function of ε is reconstructed from histogram bins.

These numerical advantages carry over to the PBE predictions. Fig. 7 shows the time evolution of the Sauter mean diameter, $d_{32}(t)$, obtained by evaluating Eq. (8) with each approach for the same breakup model and operating condition. The PDF-based results do not exhibit clear bin convergence even at $N = 1000$, with noticeable differences in both the transient and the steady values. In contrast, the results obtained using the cumulative distribution of ε converge at about 50 quadrature nodes, yielding overlapping $d_{32}(t)$ profiles and steady values consistent with the finest PDF discretization. Overall, the CDF formulation provides a more robust and efficient evaluation of Eq. (8), with reduced quadrature noise and minimal sensitivity to PDF binning. Based on these results, Gauss–Legendre quadrature with 50 nodes is adopted for the remainder of this work.

5.2. Comparison between different daughter distribution functions

Fig. 8 compares experimental cumulative drop size distributions with numerical predictions obtained using the U-shaped, bell-shaped, and 20-fragment daughter distribution functions shown in Fig. 3. For the oil_1 dispersion, the experimental CDFs have similar shapes at all impeller speeds and shift towards smaller d as the rotation rate increases. The oil_3 dispersion shows a different trend: a plateau emerges in the small-d region, indicating a substantial population of satellite drops. At 500 rpm, the plateau extends approximately from 10 to 13 μm and corresponds to CDF values around 10%, whereas at 700 rpm it extends from 7 to 11 μm with CDF values around 5%. None of the considered DDFs reproduces this plateau.

From a modelling perspective, the U-shaped and M-shaped DDFs show identical predictions under the present operating conditions. The bell-shaped and 20-fragment DDFs overlap at higher CDF values (>0.6). For CDF values above 0.8, all DDFs provide similar predictions, systematically shifted towards smaller diameters relative to the experiments. The U-shaped and M-shaped DDFs better match the CDF slope over $0.2 < \text{CDF} < 0.8$, although they generally underestimate drop sizes, particularly at higher viscosities. The bell-shaped DDF predicts narrower distributions, underestimating both the fraction of small drops and the fraction of large drops. The proposed DDF increases the fraction of small daughter drops, producing a longer left tail. This improves qualitative agreement for the oil_3 dispersion but overestimates the small-d tail for the oil_1 dispersion. Despite this improvement, the proposed DDF does not reproduce the plateau observed experimentally.

Fig. 9 summarizes the comparison between experimental and numerical values of the number-weighted mean diameter d_{10}, the Sauter mean diameter d_{32}, and the mass-weighted mean diameter d_{43}. Experimental error bars correspond to the 16th to 84th percentile range obtained from Monte Carlo resampling (see Section 2). Only one curve is shown for the U-shaped and M-shaped DDFs, as they yield identical results. For d_{10}, shown in Fig. 9(a), the bell-shaped and U-shaped DDFs reproduce the experimental trends for the oil_1 dispersion, whereas the 20-fragment DDF does not. The closest agreement is obtained for the oil_2 dispersion, where the 20-fragment DDF captures both the trend and the absolute magnitude. For the oil_3 dispersion, the 20-fragment DDF again performs best overall, although discrepancies remain at 500 rpm. Because d_{10} is number-weighted and therefore sensitive to the fine-drop population, overprediction of d_{10} indicates an overestimation

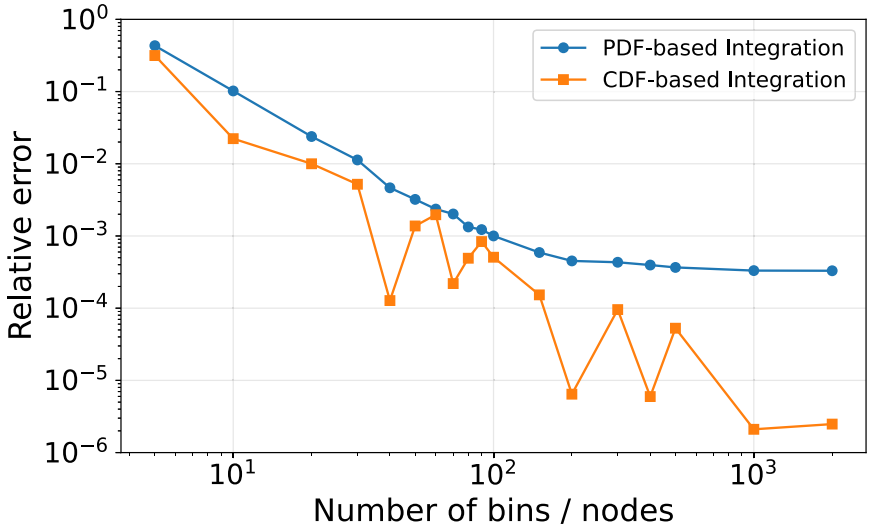

Fig. 6. Relative error in the averaged breakup frequency $\bar{h}(d)$ as a function of the discretization of the turbulent dissipation rate distribution. The PDF-based evaluation follows Buffo et al. (2016) and uses N histogram bins. The CDF-based evaluation uses Gauss–Legendre quadrature with a prescribed number of nodes.

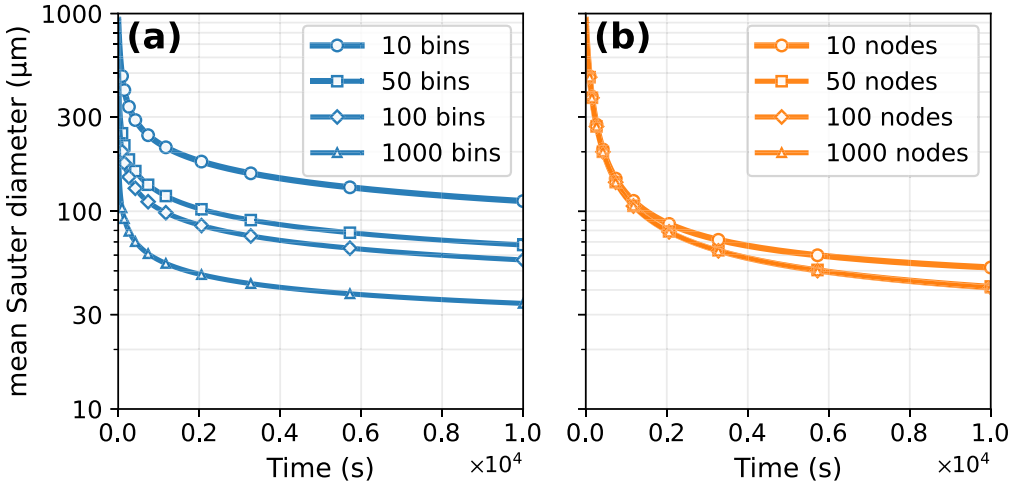

Fig. 7. Time evolution of the Sauter mean diameter $d_{32}(t)$ obtained from the population balance solved with (a) PDF- and (b) CDF-based quadratures using different discretizations.

of the mean size of the small-drop population, which may lead to underestimation of emulsion stability.

For d_{32}, Fig. 9(b), all DDFs predict similar trends for the oil_1 and oil_3 dispersions, also showing good quantitative agreement at the lowest viscosity, with deviations on the order of 5%. At high viscosity, simulations consistently underestimate d_{32}, most probably due to an underprediction of the number of large drops. The proposed DDF performs slightly worse than the bell-shaped one, as the increased production of small daughters has limited influence on d_{32}, which scales with the square of the droplet diameter.

For d_{43}, Fig. 9(c), the trend with impeller speed is captured by all DDFs, but absolute values are consistently underestimated, particularly at 100 cSt. Because d_{43} is mass-weighted, this indicates an underprediction of large drops. Such discrepancies may lead to overestimation of mixture homogeneity in engineering modelling, since large drops are more prone to segregation.

5.3. Comparison of number-based PDFs

Fig. 10 shows the number-based drop size probability density functions for the three viscosities at 700 rpm, normalized by the corresponding maximum Kolmogorov–Hinze diameter ($d_H = 193\,\mu m$). Experimentally, the oil_1 dispersion exhibits a unimodal distribution with a narrow peak shifting towards smaller d as rotation increases. The oil_2 dispersion becomes distinctly bimodal, with one peak at small diameters corresponding to satellite drops a few percent of the Kolmogorov–Hinze diameter. With the oil_3 dispersion, multiple peaks appear, forming a broad distribution which spans nearly three orders of magnitude. In all cases, the largest observed drop diameters are comparable to d_H: approximately 0.7 d_H at low viscosity and up to 5 d_H at high viscosity. This confirms that the Kolmogorov–Hinze diameter remains a useful reference for the maximum stable size under turbulent breakup.

Across all viscosities, the numerical DDFs predict similar distribution shapes, with limited sensitivity to dispersed-phase viscosity. Conversely, the experimental distributions vary markedly with viscosity, indicating that the breakup kernels, although incorporating viscosity effects, may underestimate their influence. The bell-shaped DDF reproduces the oil_1 dispersion case well but fails to capture the secondary peaks or broad distributions observed at higher viscosities. The U-shaped DDF yields similar peak positions but more skewed shapes. The proposed DDF produces a bimodal distribution that improves agreement for the oil_3 dispersion by generating a longer left tail, but it does not reproduce the secondary peak observed in the oil_2 dispersion or the narrow unimodal distribution in the oil_1 dispersion. All DDFs

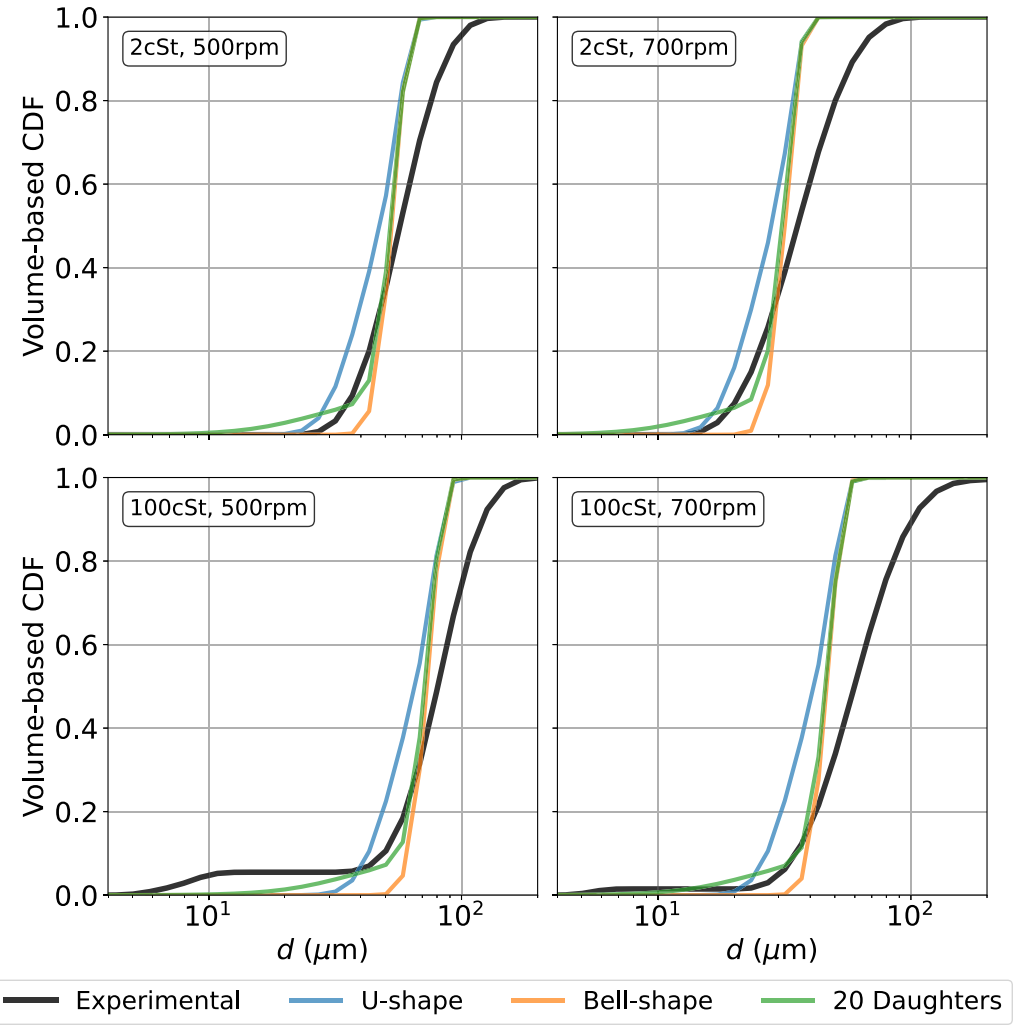

Fig. 8. Volume-based cumulative distribution functions for different viscosities and impeller speeds, obtained experimentally and from PBE simulations using different DDFs.

predict maximum drop diameters around 0.3–0.4 d_H, underestimating the upper tail, particularly in viscous systems.

The observed numerical trends align with the regimes reported by Carrillo De Hert and Rodgers (2018): accurate predictions are obtained at low dispersed-phase viscosity, where the DSD remains narrow and dominated by inertial breakup. The discrepancies increase at intermediate viscosity, where the distributions broaden and become weakly bimodal, and become largest at high viscosity, where satellite-rich left tails dominate the DSD. In this high-viscosity regime, the breakup-only model underpredicts both the small-drop plateau and the large-drop right tail. This suggests that the adopted breakup frequency may underestimate the resistance of viscous drops to deformation, particularly in the large-drop tail. Coalescence among the numerous small fragments produced at high dispersed-phase viscosity may also affect the steady-state DSD, even at the dilute global volume fraction considered here. However, the present experiments were designed to assess breakup under dilute conditions, not to separate breakup and coalescence contributions. Including coalescence would require additional closures for collision frequency and coalescence efficiency, introducing modelling choices that cannot be tested independently with the available steady-state DSDs. It would therefore be difficult to determine whether differences between predictions and experiments arise from the adopted breakup frequency, from the daughter distribution function, or from the coalescence description. The proposed DDF improves the prediction of the left tail by enabling multimodality and asymmetric fragment distributions, but it cannot compensate for inaccuracies originating from the breakup frequency. Targeted single-drop or local-swarm experiments, or numerical simulations resolving daughter size distributions at different viscosity ratios, would be required to determine its parameters more reliably across operating conditions.

The role of continuous-phase viscosity also remains outside the scope of the present dataset. All experiments were performed with water as the continuous phase, while only dispersed-phase viscosity and impeller speed were varied. The available data therefore do not allow the effect of continuous-phase viscosity on the breakup frequency to be assessed. Although previous studies show that increasing continuous-phase viscosity can change the breakup pathway, a quantitative extension of the breakup frequency to account for this effect would require dedicated experiments in which the continuous-phase viscosity is varied systematically.

These results also clarify the intended role of the model. At its present level of closure, the model should be regarded primarily as a tool for analysing breakup kernels and daughter distribution functions, rather than as a final design model for liquid–liquid dispersions. Similar volume-averaged population balance models have provided useful predictions when the relevant turbulent scales are appropriately represented (Buffo et al., 2016; Maluta et al., 2021b; Raponi et al., 2023; Maluta et al., 2025). The present model has the additional advantage of retaining the full drop size distribution at low computational cost, allowing direct comparison with measured distributions. If the

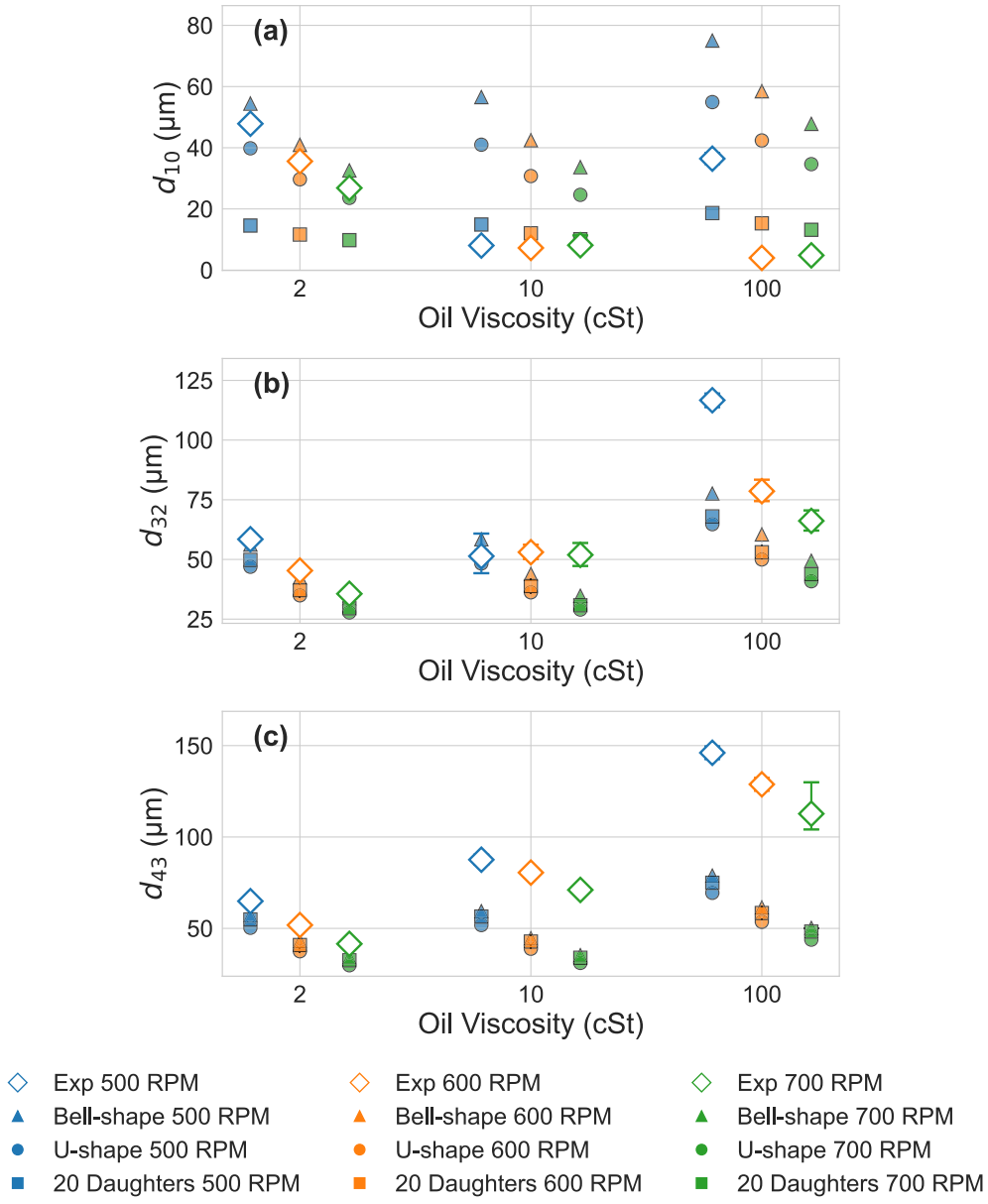

Fig. 9. Comparison between experimental and numerical mean diameters obtained using different DDFs for all investigated viscosities and impeller speeds. (a) d_{10}, (b) d_{32}, (c) d_{43}.

objective is limited to a few selected moments or their ratios, such as d_{32}, moment methods, including quadrature-based moment methods (Marchisio and Fox, 2013), may be more computationally efficient; the present approach is instead useful when the distribution shape, the small-drop tail, and the large-drop tail are included in the model assessment.

6. Conclusions

A volume-averaged population balance model has been developed to describe drop breakup in turbulent liquid–liquid dispersions in mechanically agitated systems. The model solves the population balance equation for a spatially homogeneous drop size distribution, while the spatial variability of turbulent dissipation rate is retained through the distribution obtained from CFD. The model introduces two main improvements with respect to previous volume-averaged formulations: (i) the turbulent dissipation rate distribution is included through its cumulative distribution function, avoiding the reconstruction of a binned probability density function, and (ii) the daughter distribution function is written as a weighted sum of two beta distributions, so that asymmetric and multimodal daughter distributions can be represented while preserving mass. In the evaluation of the breakup kernel, the cumulative distribution formulation reduced the numerical error by about two orders of magnitude relative to the probability density approach and required fewer than fifty quadrature nodes to obtain discretization-independent results. The proposed daughter distribution function provides additional flexibility in the production of small fragments, which is particularly relevant at high dispersed-phase viscosity, where standard distribution shapes do not reproduce the experimentally observed left tail dominated by satellite drops.

A comprehensive experimental dataset was collected over multiple impeller speeds and dispersed-phase viscosities, providing full drop size distributions rather than only averaged metrics. This enabled a comparison with both distribution features and integral quantities such as d_{10}, d_{32}, and d_{43}. The trends with viscosity and rotation rate are consistent with empirical regimes reported in the literature (Carrillo De Hert and Rodgers, 2018, 2019), including the emergence of satellite drops at high dispersed-phase viscosity. At low viscosity, the adopted

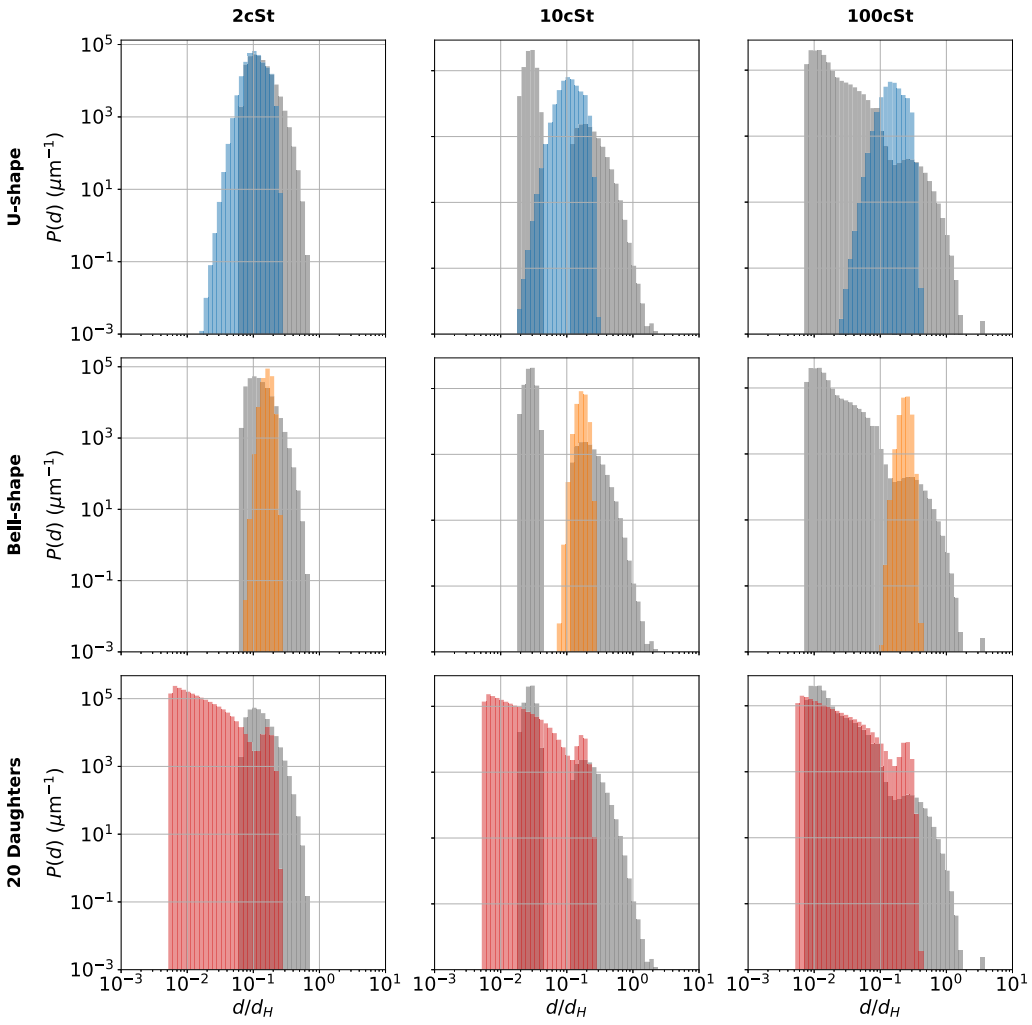

Fig. 10. Number-based drop size probability density functions obtained experimentally, shown in grey, and from PBE simulations using different DDFs at 700 rpm. The abscissa is normalized by the maximum Kolmogorov–Hinze diameter.

breakup kernel combined with standard DDF shapes from the literature provides the closest overall agreement with the experiments, consistent with a predominantly inertial breakup regime. At higher viscosity, discrepancies emerge in the distribution shape and in the mean diameter metrics, with the largest deviations occurring when satellite drops produce an extended left tail. A two-beta DDF was therefore introduced to improve the representation of the small-diameter region. While this improves agreement in the left tail, remaining discrepancies indicate that further improvements must also address the breakup frequency model.

The systematic underprediction of the right-hand tail across all models suggests that this discrepancy is unlikely to originate from the DDF alone. It is more consistent with limitations of the present breakup-only description: the adopted breakup frequency may underestimate viscous resistance to deformation, while coalescence among the many small fragments produced at high viscosity may also affect the steady-state DSD. While coalescence is often expected to be weak at low dispersed-phase loading, it may become relevant even at the 0.1 vol% conditions considered here when many small fragments are produced. Dedicated experiments measuring daughter size distributions and breakup frequencies at high viscosity ratios would be required to refine the breakup kernel and to determine the proposed DDF parameters quantitatively.

Future work will extend the experimental conditions investigated in this study, together with the modelling framework, to higher dispersed-phase loadings, where coalescence can be assessed more directly, and to systems with varying continuous-phase viscosity, so that its effect on the breakup frequency can be quantified and validated. From a methodological perspective, the proposed model is compatible with turbulent dissipation rate distributions obtained from Large Eddy Simulation (LES) and Direct Numerical Simulation (DNS), and it is suitable for uncertainty quantification and design optimization of industrial emulsifiers.

CRediT authorship contribution statement

Francesco Maluta: Writing – original draft, Software, Methodology, Investigation, Data curation, Conceptualization. **Gaetano D'Avino:** Writing – review & editing, Funding acquisition, Conceptualization. **Cristian Marchioli:** Writing – review & editing, Funding acquisition, Conceptualization. **Alessandro Paglianti:** Writing – review & editing, Resources, Funding acquisition, Conceptualization. **Antonio Buffo:** Writing – review & editing, Software, Methodology, Data curation, Conceptualization.

Declaration of competing interest

The authors declare that they have no known competing financial interests or personal relationships that could have appeared to influence the work reported in this paper.

Acknowledgements

The financial support of the Italian Ministry of University and Research (MUR) under the program "Progetti di Rilevante Interesse Nazionale", Grant 20229WJBPS, is gratefully acknowledged. The authors thank Giuseppina Montante and Daniele Marchisio for helpful discussions and constructive feedback on this work.

Data availability

Software and dataset to reproduce the reported results are available at https://doi.org/10.5281/zenodo.18715777.

References

Alopaeus, V., Koskinen, J., Keskinen, K.I., Majander, J., 2002. Simulation of the population balances for liquid-liquid systems in a nonideal stirred tank. Part 2-parameter fitting and the use of the multiblock model for dense dispersions. Chem. Eng. Sci. 57 (10), 1815–1825, Cited by: 195.

Baldi, S., Ducci, A., Yianneskis, M., 2004. Determination of dissipation rate in stirred vessels through direct measurement of fluctuating velocity gradients. Chem. Eng. Technol.: Ind. Chem.-Plant Equip.-Process Eng.-Biotechnol. 27 (3), 275–281.

Bałdyga, J., Bourne, J.R., 1992. Interactions between mixing on various scales in stirred tank reactors. Chem. Eng. Sci. 47 (8), 1839–1848.

Bana, G., Lamadie, F., Charton, S., Randriamanantena, T., Lucor, D., Sheibat-Othman, N., 2024. BYG-drop: a tool for enhanced droplet detection in liquid–liquid systems through machine learning and synthetic imaging. Front. Chem. Eng. 6, 1415453.

Becker, P.J., Puel, F., Chevalier, Y., Sheibat-Othman, N., 2014. Monitoring silicone oil droplets during emulsification in stirred vessel: Effect of dispersed phase concentration and viscosity. Can. J. Chem. Eng. 92 (2), 296–306.

Buffo, A., De Bona, J., Vanni, M., Marchisio, D., 2016. Simplified volume-averaged models for liquid-liquid dispersions: Correct derivation and comparison with other approaches. Chem. Eng. Sci. 153, 382–393.

Burke, I., Dhayaparan, T., Youssef, A.S., Schmidt, K., Kockmann, N., 2024. Two deep learning methods in comparison to characterize droplet sizes in emulsification flow processes. J. Flow Chem. 14 (4), 597–613.

Calabrese, R.V., Chang, T.P.K., Dang, P.T., 1986. Drop breakup in turbulent stirred-tank contactors. Part I: Effect of dispersed-phase viscosity. AIChE J. 32 (4), 657–666.

Carrillo De Hert, S., Rodgers, T.L., 2018. On the steady-state drop size distribution in stirred vessels. Part I: Effect of dispersed phase viscosity. AIChE J. 64 (9), 3293–3302.

Carrillo De Hert, S., Rodgers, T.L., 2019. On the steady-state drop size distribution in stirred vessels. Part II: Effect of continuous phase viscosity. AIChE J. 65 (5), e16556.

Clark, N.N., 1988a. Drop breakup in a turbulent flow—I. Conceptual and modeling considerations. Chem. Eng. Sci. 43 (3), 671–682.

Clark, N.N., 1988b. Drop breakup in a turbulent flow—II. Turbulent emulsification experiments in a grid-impeller vessel. Chem. Eng. Sci. 43 (3), 683–691.

Coulaloglou, C.A., Tavlarides, L.L., 1977. Description of interaction processes in agitated liquid–liquid dispersions. Chem. Eng. Sci. 32 (11), 1289–1297.

Davies, J.T., 1987. A physical interpretation of drop sizes in homogenizers and agitated vessels. Chem. Eng. Sci. 42 (7), 1671–1683.

Desnoyer, C., Masbernat, O., Gourdon, C., 2003. Experimental study of drop size distributions at high phase ratio in liquid–liquid dispersions. Chem. Eng. Sci. 58 (7), 1353–1363.

EL-Hamouz, A., Cooke, M., Kowalski, A., Sharratt, P., 2009. Dispersion of silicone oil in water surfactant solution: Effect of impeller speed, oil viscosity and addition point on drop size distribution. Chem. Eng. Process.: Process. Intensif. 48 (2), 633–642.

Escudié, R., Liné, A., 2003. Experimental analysis of hydrodynamics in a radially agitated tank. AIChE J. 49 (3), 585–603.

Farsoiya, P.K., Liu, Z., Daiss, A., Fox, R.O., Deike, L., 2023. Role of viscosity in turbulent drop break-up. J. Fluid Mech. 972, A11.

Ghanem, R.G., Doostan, A., 2006. On the construction and analysis of stochastic models: Characterization and propagation of the errors associated with limited data. J. Comput. Phys. 217 (1), 63–81.

Grace, H.P., 1982. Dispersion phenomena in high viscosity immiscible fluid systems and application of static mixers as dispersion devices in such systems. Chem. Eng. Commun. 14 (3–6), 225–277.

Håkansson, A., 2020. On the validity of different methods to estimate breakup frequency from single drop experiments. Chem. Eng. Sci. 227, 115908.

Hardy, A., Nil, P., Hervé, R., Fabrice, L., Tojonirina, R., Éric, O., 2025. Influence of continuous phase viscosity on drop breakup mechanisms in a miniature cubic mixer at moderate Reynolds numbers. Chem. Eng. Sci. 122751.

Hinze, J.O., 1955. Fundamentals of the hydrodynamic mechanism of splitting in dispersion processes. AIChE J. 1 (3), 289–295.

Illingworth, J., Kittler, J., 1988. A survey of the Hough transform. Comput. Vis. Graph. Image Process. 44 (1), 87–116.

Ilonen, J., Juránek, R., Eerola, T., Lensu, L., Dubská, M., Zemčík, P., Kälviäinen, H., 2018. Comparison of bubble detectors and size distribution estimators. Pattern Recognit. Lett. 101, 60–66.

Khalil, A., Puel, F., Chevalier, Y., Galvan, J.-M., Rivoire, A., Klein, J.-P., 2010. Study of droplet size distribution during an emulsification process using in situ video probe coupled with an automatic image analysis. Chem. Eng. J. 165 (3), 946–957.

Kraume, M., Gäbler, A., Schulze, K., 2004. Influence of physical properties on drop size distribution of stirred liquid-liquid dispersions. Chem. Eng. Technol.: Ind. Chem.stry-Plant Equip.-Process Eng.-Biotechnol. 27 (3), 330–334.

Krizhevsky, A., Sutskever, I., Hinton, G.E., 2017. ImageNet classification with deep convolutional neural networks. Commun. ACM 60 (6), 84–90.

Laurenzi, F., Coroneo, M., Montante, G., Paglianti, A., Magelli, F., 2009. Experimental and computational analysis of immiscible liquid–liquid dispersions in stirred vessels. Chem. Eng. Res. Des. 87 (4), 507–514.

Lehr, F., Millies, M., Mewes, D., 2002. Bubble-size distributions and flow fields in bubble columns. AIChE J. 48 (11), 2426–2443.

Liao, Y., Lucas, D., 2009. A literature review of theoretical models for drop and bubble breakup in turbulent dispersions. Chem. Eng. Sci. 64 (15), 3389–3406.

Lohse, D., Zhang, X., 2020. Physicochemical hydrodynamics of droplets out of equilibrium. Nat. Rev. Phys. 2, 426–443.

Luo, H., Svendsen, H.F., 1996. Theoretical model for drop and bubble breakup in turbulent dispersions. AIChE J. 42 (5), 1225–1233.

Maaß, S., Gäbler, A., Zaccone, A., Paschedag, A., Kraume, M., 2007. Experimental investigations and modelling of breakage phenomena in stirred liquid/liquid systems. Chem. Eng. Res. Des. 85 (5), 703–709.

Maaß, S., Kraume, M., 2012. Determination of breakage rates using single drop experiments. Chem. Eng. Sci. 70, 146–164.

Maaß, S., Metz, F., Rehm, T., Kraume, M., 2010. Prediction of drop sizes for liquid–liquid systems in stirred slim reactors—Part I: Single stage impellers. Chem. Eng. J. 162 (2), 792–801.

Maaß, S., Wollny, S., Voigt, A., Kraume, M., 2011. Experimental comparison of measurement techniques for drop size distributions in liquid/liquid dispersions. Exp. Fluids 50 (2), 259–269.

Maluta, F., Alberini, F., Paglianti, A., Montante, G., 2025. Characterization of bubble breakup mechanisms in non-coalescing electrolyte solutions. Int. J. Multiph. Flow 105471.

Maluta, F., Buffo, A., Marchisio, D., Montante, G., Paglianti, A., Vanni, M., 2021a. Effect of turbulent kinetic energy dissipation rate on the prediction of droplet size distribution in stirred tanks. Int. J. Multiph. Flow 136, 103547.

Maluta, F., Buffo, A., Marchisio, D., Montante, G., Paglianti, A., Vanni, M., 2021b. Numerical and experimental analysis of the daughter distribution in liquid-liquid stirred tanks. Chem. Eng. Technol. 44, 1994–2001.

Maluta, F., D'Avino, G., Marchioli, C., Paglianti, A., Buffo, A., 2026. Software and dataset for paper "Improving simplified models for liquid-liquid dispersions using detailed numerical and experimental data". http://dx.doi.org/10.5281/zenodo.18715777.

Maluta, F., Montante, G., Paglianti, A., 2020. Analysis of immiscible liquid-liquid mixing in stirred tanks by electrical resistance tomography. Chem. Eng. Sci. 227, 115898.

Marchisio, D.L., Fox, R.O., 2013. Computational Models for Polydisperse Particulate and Multiphase Systems. Cambridge University Press.

Martínez-Bazán, C., Montañes, J.L., Lasheras, J.C., 1999. On the breakup of an air bubble injected into a fully developed turbulent flow. Part 1. Breakup frequency. J. Fluid Mech. 401, 157–182.

Peterson, J.D., Bagkeris, I., Michael, V., 2022. A new framework for numerical modeling of population balance equations: Solving for the inverse cumulative distribution function. Chem. Eng. Sci. 259, 117781.

Podgórska, W., 2006. Modelling of high viscosity oil drop breakage process in intermittent turbulence. Chem. Eng. Sci. 61 (9), 2986–2993.

Qi, Y., Masuk, A.U.M., Ni, R., 2020. Towards a model of bubble breakup in turbulence through experimental constraints. Int. J. Multiph. Flow 132, 103397.

Ramkrishna, D., 2000. Population Balances: Theory and Applications to Particulate Systems in Engineering. Academic Press, San Diego.

Raponi, A., Achermann, R., Romano, S., Trespi, S., Mazzotti, M., Cipollina, A., Buffo, A., Vanni, M., Marchisio, D., 2023. Population balance modelling of magnesium hydroxide precipitation: Full validation on different reactor configurations. Chem. Eng. J. 477, 146540.

Ribeiro, M.M., Regueiras, P.F., Guimaraes, M.M.L., Madureira, C.M.N., Cruz-Pinto, J.J.C., 2011. Optimization of breakage and coalescence model parameters in a steady-state batch agitated dispersion. Ind. Eng. Chem. Res. 50 (4), 2182–2191.

Rochman, D., Zwermann, W., Van Der Marck, S., Koning, A., Sjöstrand, H., Helgesson, P., Krzykacz-Hausmann, B., 2014. Efficient use of Monte Carlo: Uncertainty propagation. Nucl. Sci. Eng. 177 (3), 337–349.

Rodriguez, O., Angeli, P., Legendre, D., Climent, E., Soldati, A., 2025. Drop laden flows. Int. J. Multiph. Flow 191, 105284.

Singh, K., Mahajani, S., Shenoy, K., Ghosh, S., 2008. Representative drop sizes and drop size distributions in A/O dispersions in continuous flow stirred tank. Hydrometallurgy 90 (2–4), 121–136.

Singh, K., Mahajani, S., Shenoy, K., Ghosh, S., 2009. Population balance modeling of liquid- liquid dispersions in homogeneous continuous-flow stirred tank. Ind. Eng. Chem. Res. 48 (17), 8121–8133.
Solsvik, J., Jakobsen, H.A., 2015. Single drop breakup experiments in stirred liquid–liquid tank. Chem. Eng. Sci. 131, 219–234.
Solsvik, J., Tangen, S., Jakobsen, H.A., 2013. On the constitutive equations for fluid particle breakage. Rev. Chem. Eng. 29 (5), 241–356.
Stamatoudis, M., Tavlarides, L.L., 1985. Effect of continuous-phase viscosity on the drop sizes of liquid-liquid dispersions in agitated vessels. Ind. Eng. Chem. Process. Des. Dev. 24 (4), 1175–1181.
Triballier, K., Dumouchel, C., Cousin, J., 2003. A technical study on the Spraytec performances: influence of multiple light scattering and multi-modal drop-size distribution measurements. Exp. Fluids 35 (4), 347–356.
Yu, S., Zhou, H., Li, S., Chen, Z., Wang, Y., 2025. Proper definition and mechanism of droplet breakage frequency - Discussion and clarification. Chem. Eng. Sci. 306, 121302.
Zhao, H., Ge, W., 2007. A theoretical bubble breakup model for slurry beds or three-phase fluidized beds under high pressure. Chem. Eng. Sci. 62 (1–2), 109–115.
Zhou, H., Jing, S., Fang, Q., Li, S., Lan, W., 2017. Direct measurement of droplet breakage in a pulsed disc and doughnut column. AIChE J. 63 (9), 4188–4200.
Zhou, H., Yu, X., Jing, S., Zhou, H., Lan, W., Li, S., 2019. Measurement of droplet breakage in a pump-mixer. Chem. Eng. Sci. 195, 23–38.
Zhou, H., Yu, X., Wang, B., Jing, S., Lan, W., Li, S., 2021a. Experimental study on drop breakup time and breakup rate with drop swarms in a stirred tank. AIChE J. 67 (1), e17065.
Zhou, H., Yu, X., Wang, B., Jing, S., Lan, W., Li, S., 2021b. Modeling study on drop breakup time in turbulent dispersions. Chem. Eng. Sci. 238, 116599.
Zhou, H., Yu, X., Wang, B., Jing, S., Lan, W., Li, S., 2022. Breakup model of oscillating drops in turbulent flow field. Chem. Eng. Sci. 247, 117036.